Mechanism of Interaction between the General Anesthetic Halothane and a Model Ion Channel Protein, I: Structural Investigations via X-Ray Reflectivity from Langmuir Monolayers

Joseph Strzalka,[†] Jing Liu,[†] Andrey Tronin,[†] Inna Y. Churbanova,[†] Jonas S. Johansson,[‡] and J. Kent Blasie[†*]

[†]Department of Chemistry, University of Pennsylvania, Philadelphia, Pennsylvania; and [‡]Department of Anesthesiology and Critical Care, University of Pennsylvania, Philadelphia, Pennsylvania

ABSTRACT   We previously reported the synthesis and structural characterization of a model membrane protein comprised of an amphiphilic 4-helix bundle peptide with a hydrophobic domain based on a synthetic ion channel and a hydrophilic domain with designed cavities for binding the general anesthetic halothane. In this work, we synthesized an improved version of this halothane-binding amphiphilic peptide with only a single cavity and an otherwise identical control peptide with no such cavity, and applied x-ray reflectivity to monolayers of these peptides to probe the distribution of halothane along the length of the core of the 4-helix bundle as a function of the concentration of halothane. At the moderate concentrations achieved in this study, approximately three molecules of halothane were found to be localized within a broad symmetric unimodal distribution centered about the designed cavity. At the lowest concentration achieved, of approximately one molecule per bundle, the halothane distribution became narrower and more peaked due to a component of ~19Å width centered about the designed cavity. At higher concentrations, approximately six to seven molecules were found to be uniformly distributed along the length of the bundle, corresponding to approximately one molecule per heptad. Monolayers of the control peptide showed only the latter behavior, namely a uniform distribution along the length of the bundle irrespective of the halothane concentration over this range. The results provide insight into the nature of such weak binding when the dissociation constant is in the mM regime, relevant for clinical applications of anesthesia. They also demonstrate the suitability of both the model system and the experimental technique for additional work on the mechanism of general anesthesia, some of it presented in the companion parts II and III under this title.

INTRODUCTION

The mechanism of general anesthesia defies elucidation despite more than a century and a half of practical application. A variety of small molecules are capable of producing the anesthetic effect, undermining any apparent structure-activity relationship (1). Their most notable common characteristic is the way in which their anesthetic potency correlates with their solubility in nonpolar media, long known as the Meyer-Overton Rule, and pointing to membranes as the site of anesthetic action (2). Although indirect mechanisms continue to be proposed, there is growing evidence for a direct mechanism, in which anesthetics interact with specific sites in membrane proteins (3). The putative targets are ligand-gated ion channels central to neurological signal transmission (3). The three-dimensional structure of one representative ligand-gated ion channel, the acetylcholine receptor, is now known from cryo-electron microscopy studies (4), but structural information regarding its interaction with an anesthetic may continue to present a challenge to both electron microscopy and x-ray crystallography, because only relatively weak binding of the anesthetic characterized by a submillimolar dissociation constant is of physiological relevance (1,5). This lack of structural information hinders the development of the theory of direct mechanism of anesthetic action.

An alternative approach to studying protein/anesthetic interactions is the use of model proteins, so-called maquettes, namely synthetic peptides based on simple and robust structural motifs (6), which may be designed with cavities for binding anesthetics (7). The first implementation of this strategy used amphipathic α-helical peptides generated by a heptad-repeat pattern with a majority of hydrophilic residues and a minority of hydrophobic residues. After homodimerization, the dihelical units assembled in an antitopology to form soluble 4-helix bundles with the hydrophobic residues buried in the core of the bundle. The replacement of a bulkier Leu residue with a smaller Ala residue at a selected site in the primary sequence located in the bundle's interior coupled with the antitopology of the bundle resulted in two cavities capable of binding the representative anesthetic halothane ($F_3CCBrClH$) with a dissociation constant of 0.7 mM (7), near the clinically relevant range, with the halothane titration monitored by fluorescence quenching of Trp residues adjacent to the designed binding cavities. Subsequent optimization of the sequence further reduced the dissociation constant to 200 μM (8), closely matching the clinically effective concentration of halothane ($EC_{50} = 250$ μM). NMR studies of this optimized soluble peptide recently yielded the solution structure of this peptide in the presence of one halothane per bundle, revealing that the halothane was bound, however, in an unexpected location in the center of the bundle between

the two layers of Trp residues distinctly apart from the designed binding cavities located nearer each end of the bundle (9). Although further work continues on such water-soluble bundles, they have inherent limitations that will prevent them from mimicking many of the properties of ligand-gated ion channels.

This work results from a different implementation of the maquette peptide approach using amphiphilic 4-helix bundles (10). The design was based on that of the soluble anesthetic-binding 4-helix bundle, with the sequence extended by two heptads possessing a majority of hydrophobic residues and a minority of hydrophilic residues. The resulting α-helices are covalently homodimerized and assemble to form 4-helix bundles with a *syn* topology, making the exterior of one end of the bundle hydrophilic and the exterior of the other end hydrophobic. We designated the peptide hbAP0 (halothane-binding amphiphilic peptide 0). Within the hydrophilic domain of the bundle, each helix has a Trp residue with an Ala residue at an interior position on either side of the Trp, so that, like its soluble predecessor, two cavities for binding anesthetics are formed. Within the hydrophobic domain of the bundle, the majority hydrophobic sequence is inspired by a synthetic ion channel (11), hence the amphiphilic anesthetic-binding peptide is designed to be a model ion channel; although this functionality has not yet been demonstrated. Several demonstrated properties of the amphiphilic peptide bundle make it an interesting model system. First, the peptide binds halothane, albeit with a dissociation constant of ~3 mM, somewhat larger than that of the soluble peptide. Second, the amphiphilic peptide bundles can be spread from methanol solution to form Langmuir monolayers at the air/water interface in the absence of lipid (10). Third, x-ray reflectivity measurements showed that the application of surface pressure could orient the ensemble of peptide molecules with the α-helices oriented normal to the air/water interface (10). Fourth, x-ray scattering measurements verify that the peptide maintains its 4-helix coiled-coil structure at the air-water interface (12). On the strength of these advantages, we sought to follow up our earlier structural investigations of the *apo* peptide with a structural study of the peptide interacting with halothane.

Because of the high electron density of the halogen-rich halothane molecule, we expected it would have sufficient contrast relative to peptide and water that its presence within a Langmuir monolayer should be observable by x-ray reflectivity measurements. Because the orientation of the peptide bundles at high surface pressures essentially maps the sequence of amino acids onto the coordinate axis normal to the air/water interface, the direction probed by x-ray reflectivity, we expected to be able to determine the location of any halothane bound to the bundle and infer which amino-acid residues interact with the halothane. For this purpose, we synthesized a new amphiphilic halothane-binding peptide by making two substitutions in the sequence of the first peptide (10). Our new peptide, hbAP1, is hbAP0(A8L,L22M). Putting

Leu at position 8 removes one of the binding cavities in the bundle, leaving only a single binding site, Ala^{19}, facilitating interpretation of the results. Introducing Met allows for future labeling experiments with Se-Met. We also synthesized a control peptide, hbAP1(A19L), which has no designed cavity for binding halothane. As a preliminary to our x-ray reflectivity study of monolayers of these peptides in the presence of halothane, we report the characterization of these peptides solubilized in aqueous buffer with the aid of detergent and at the air/water interface in the absence of halothane. The results show hbAP1 has an affinity for halothane (K_d = 2.5 mM), similar to that of hbAP0. Just like hbAP0, the peptides form stable monolayers at the air/water interface above an aqueous subphase, can be similarly oriented through the application of surface pressure, and maintain their 4-helix coiled-coil conformation at the air/water interface. But our main purpose here is to report on x-ray reflectivity measurements conducted on Langmuir monolayers of these peptides in equilibrium with a gaseous superphase containing halothane vapor.

A majority of this work concerns x-ray reflectivity measurements to study the dissociation of halothane from our peptides. In brief, we formed Langmuir monolayers of the vectorially oriented halothane-binding peptide hbAP1 or of the vectorially oriented control peptide hbAP1(A19L) without the designed binding cavity. For each monolayer, we collected x-ray reflectivity data in the absence of the anesthetic, after introduction of maximal halothane vapor in the gaseous superphase above the monolayer, and subsequently after stepwise purges of the halothane from the monolayer system that reduced the atmospheric concentration of halothane back to zero. The reflectivity data showed significant, reproducible effects due to the presence of halothane that were mostly reversible. We applied a model-independent means of analysis to obtain the monolayer profile structure, the average electron-density distribution projected onto the coordinate axis normal to the air/water interface, for each monolayer under the different concentrations of halothane. The results for the hbAP1 peptide in these dissociation experiments achieved only moderate concentrations of three to four halothane molecules per bundle. However, they provide evidence for localization of the halothane within a broad symmetric unimodal distribution centered on the site of the designed cavity, whereas at higher concentrations the distribution becomes spread uniformly along the entire length of the bundle. Recent experiments investigated the "association" of halothane with the peptides, exposing the monolayer to minimal halothane concentrations in the superphase followed by a purge to zero halothane, and achieved lower concentrations of about one halothane molecule per bundle. In this case, the halothane distribution became narrower and more peaked due to a component of only ~19 Å width centered about the designed cavity. In the monolayers of the control peptide, the distribution of halothane remains uniformly distributed along the length of the bundle failing to become localized at any concentration of halothane in both the dissociation and association

experiments. These results give insight into the nature of such weak binding when the dissociation constant of the interaction is in the mM range. The consequences for understanding anesthesia and the prospects for future studies are discussed. The demonstrated utility of these oriented model protein systems has already lead to complementary studies by fluorescence and polarized infrared spectroscopy (13) and correlated molecular dynamics simulations (14) appearing in the companion parts II and III under this title.

METHODS

Peptides

hbAP0

Ac-LKKLREE AAKLFEE WKKLAEE LLLLALL QLLLALL QLGGC-CONH$_2$

hbAP1

Ac-LKKLREE LAKLFEE WKKLAEE MLLLALL QLLLALL QLGGC-CONH$_2$

hbAP1(A19L)

Ac-LKKLREE LAKLFEE WKKLLEE MLLLALL QLLLALL QLGGC-CONH$_2$

The peptides with amino-acid sequences and names given above were prepared by solid phase synthesis with Fmoc chemistry as described previously (10). After dimerization via the C-terminal Cys residues, the lyophilized powder was dissolved in pure methanol at ~100 μM concentration of α-helices. The peptide hbAP0 has two designed cavities for binding halothane at the sites where Alanine is interior to the bundle (positions 8 and 19), hbAP1 has only one designed cavity for binding halothane (Ala^{19}), whereas hbAP1(A19L) is the control peptide with no designed cavity for binding halothane. The substitution L22→M in hbAP1 will allow future labeling with Se-Met to enable resonant x-ray reflectivity measurements (15) that could be used to more precisely determine the position of the cavity along the length of the bundle within the electron-density profile derived from the reflectivity data.

Halothane system

Data were collected in three separate synchrotron runs. In each run, the sample stage of the liquid surface spectrometer held a gastight canister containing the Langmuir trough. A large kapton window permitted the incident and scattered x-ray beams to penetrate the canister. A system of Teflon tubing and valves permitted the air in the canister to be purged with moist helium, as monitored by an oxygen sensor in the canister (S101, QUBIT Systems, Kingston, ON, Canada). Then the canister could be connected to a closed loop including a diaphragm pump that forced the helium through liquid halothane in a glass washing bottle, vaporizing the halothane and causing its concentration in the gas phase to increase with time. Before use, liquid halothane (Sigma-Aldrich) was filtered on an alumina column to remove the preservative thymol. A portable UV-vis spectrophotometer (SD 2000, Ocean Optics, Dunedin, FL) and a deuterium/halogen lamp (Model DH-2000, Mikropack GmbH, Germany) coupled with fiber optics to a 1-cm pathlength quartz cuvette connected to the halothane loop, were used to monitor the halothane concentration by its optical absorption. The absorption spectrum of halothane combined with the lamp output resulted in a working spectrum with a peak at 237 nm. When a steady-state concentration was reached, typically after 1–3 h, the valves were closed, sealing the canister. As the vapor pressure of halothane is 232 mmHg at 20°C, the concentration of halothane vapor cannot exceed ~1/3 atmosphere, or

a gas-phase concentration of ~16 mM. After reflectivity measurements, the canister was flushed with moist helium, and the vented gas was directed to a condenser to trap part of the halothane used and then to exhaust ventilation. Readers are cautioned that plastic components in the trough and oxygen sensor were susceptible to damage from the halothane vapor. The later experimental run used a trough with all interior components made of stainless steel or teflon. This run also replaced the conventional Wilhelmy plate surface pressure transducer used earlier (Riegler & Kirstein, Postsdam, Germany) with a Wilhelmy plate transducer with a fiber-optic readout developed in our lab. Additionally, the condenser was replaced with activated charcoal filters for trapping anesthetic gases (F-Air canisters, Braintree Scientific, Braintree, MA).

As a practical matter, the change in the transmission of x-rays through the canister containing the Langmuir trough could determine the relative concentration of halothane vapor in the moist helium atmosphere above the sample. With the trough lowered out of the path of the beam, the ratio of counts in the scintillation detector to counts in the ion chamber monitor positioned before the sample was highest in the absence of halothane and reduced as the halothane concentration increased. This seemed to work better on the first run, and not as well for the second run, when there seemed to be some instability in the measurement that caused the ratio to gradually change with time even without the introduction of halothane. Similarly, the spectrophotometric determination of the halothane concentration was made challenging by the length of time over which baseline stability was required (circa 12 h).

Monolayer preparation

Monolayers were spread from the methanol solution (~100 μM in α-helices) at the meniscus formed onto a glass capillary penetrating the subphase at an oblique angle. The subphase contained 1 mM potassium phosphate buffer with 10 mM KCl, pH 8, maintained at 22°C. After the canister was flushed with moist helium (~20 min), the monolayers were compressed at a constant speed of ~25 Å^2/α-helix/min to a final area of 100 ± 5 Å^2/helix and held at fixed area during the reflectivity data collection. The subphase was replaced completely before spreading a new monolayer.

X-ray reflectivity

The liquid surface spectrometer at bending magnet beamline X22-B of the National Synchrotron Light Source (16,17) (Brookhaven National Laboratory, Upton, NY) was used with incident x-ray wavelength $\lambda = 1.5275$ Å (first set of experiments) or $\lambda = 1.50625$ Å (second set) to collect x-ray reflectivity data as described previously (18). Data were collected over a range of photon momentum transfer $0.01 < q_z < 0.63$ Å^{-1}. In the first set of experiments, the trough was translated transverse to the beam by 1 mm, i.e., the width of the incident x-ray beam, to expose a fresh portion of the sample to the beam after each reflectivity scan and so avoid any potential radiation damage to the peptide monolayer. The smaller size of the trough used in the later sets of experiments made this impractical, but the reproducibility of successive scans under identical conditions appeared comparable, after the initial equilibration of the monolayer at each condition (see Results and Discussion).

Analysis of reflectivity data

The raw data files were reduced using C-Plot (Certified Scientific Software, Cambridge, MA), including normalization of the reflectivity data by the Fresnel function to eliminate the effects due to dynamical scattering from the water-air interface, leaving the kinematical scattering due to the presence of the peptide monolayer at the interface. Subsequent processing used Mathematica 4.2 (Wolfram Research, Champaign, IL). Working in the Distorted Wave Born Approximation, we used the so-called box-refinement algorithm, a model-independent means for solving the phase problem and obtaining the electron-density profile of the monolayer that accounts for the observed reflectivity data (19). Differences between the various monolayer electron-density profiles obtained from a particular monolayer under different conditions were computed and then fit with one or a sum of two

Gaussian functions of the form $A_i \, \text{Exp}[-(z-z_i)^2/2\sigma_i^2]$ using the Levenberg-Marquardt algorithm as implemented in Mathematica's NonlinearRegress package (20) with equal weighting for the datapoints. Uncertainties in the fit parameters are the standard errors obtained from the fits.

RESULTS

As described in the Introduction, we utilized a new peptide, hbAP1, with only one anesthetic binding cavity near the interface between the hydrophilic and hydrophobic domains (Ala[19]), as well as a control peptide with no such cavity, hbAP1(A19L), in these studies. Solution-based characterization techniques show that these peptides solubilized with the detergent n-octyl β-D-glucopyranoside have properties quite similar to the parent peptide hbAP0. Circular dichroism indicates helical content in excess of 93% (see Fig. S1 and Fig. S2 in the Supporting Material). Fluorescence quenching shows that hbAP1 binds halothane with a dissociation constant of 2.5 ± 0.2 mM (see Fig. S3). The similarities extend to the environment of the air/water interface, where both peptides form stable monolayers with similar pressure-area isotherms (see Fig. S4). X-ray reflectivity data collected from these Langmuir monolayers indicates that the peptide is oriented initially at low surface pressures with the long axes of the helices parallel to the air/water interface, whereas upon compression to high surface pressures and an area/helix approaching 100 Å², the helices become oriented with their long axes perpendicular to the interface (see Fig. S5). Grazing incidence x-ray diffraction data demonstrate that hbAP1 retains its association into 4-helix bundles adopting a coiled-coil conformation, without any further evidence of long-range ordering in the plane of the monolayer (see Fig. S6). Thus, at high surface pressures, the amphiphilic 4-helix bundle peptides within the Langmuir monolayer are vectorially oriented with their hydrophilic domain penetrating into the aqueous subphase below the water-air interface and their hydrophobic domain penetrating into the gaseous superphase above the interface.

Halothane, a halogen-rich electron-dense small molecule, produces definite and reproducible changes in the reflectivity of peptide monolayers when introduced into the atmosphere over the monolayer. Fresnel-normalized reflectivity data collected from the spread and compressed peptide monolayers show a characteristic pattern of maxima and minima in the range of photon momentum transfer $q_z < 0.2$ Å^{-1} (see Fig. S7 a, *black curve*), indicating that the helices are oriented with their long axes approximately normal to the air/water interface (10). Several successive scans showed small changes in the reflectivity data before converging to a pattern stable over subsequent successive scans, each reflectivity scan requiring a total of 60 min. We introduced halothane vapor to the gastight canister containing the trough, sealing the canister when the spectrophotometer indicated that the concentration of halothane had reached a steady state. Reflectivity scans collected at this maximum concentration of halothane, [halothane]$_{max}$, showed an increase in the amplitude of this pattern of maxima and minima, but no change

in their positions. The three successive scans collected at [halothane]$_{max}$ were all in good agreement to within the counting statistics (Fig. S7 b). We subsequently purged halothane from the canister with helium in a stepwise fashion, reducing the concentration of halothane in the superphase atmosphere by ~1/2 with each step. At each step, reflectivity scans showed changes in the reflectivity pattern initially that were then subsequently stable for successive scans. Finally, upon completion of the purge, the reflectivity data resembles the data collected before the introduction of halothane, although the amplitudes of the maxima, particularly the second at higher q_z, do not return entirely to their prehalothane values. Thus, the changes due to halothane are either not completely reversible, or insufficient time was provided despite the reproducibility of successive scans to within the noise level of the counting statistics (see Discussion).

The box-refinement algorithm allows us to determine from the Fresnel-normalized reflectivity data the electron-density profile of the monolayer at each concentration of halothane and thereby observe the changes due to the presence of halothane. Fig. 1 shows representative electron-density profiles obtained for the hbAP1 monolayer at each concentration of halothane investigated in the first set of experiments. The profile, $\rho(z)$, is the projection of the three-dimensional electron density of the monolayer, $\rho(\mathbf{r})$, parallel to the plane of
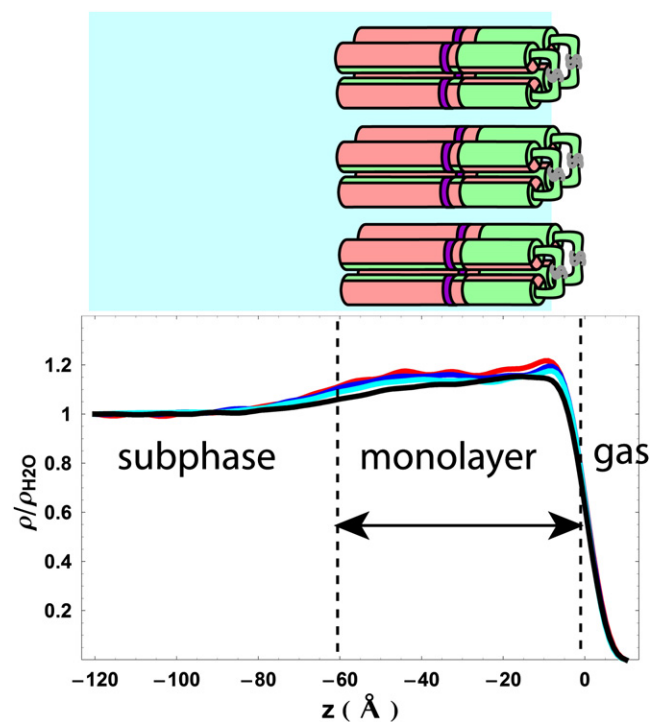

FIGURE 1 Electron-density profiles of the hbAP1 monolayer at the different concentrations of halothane established in the first set of dissociation experiments. Prehalothane (*black*), maximal halothane of [halothane]$_{max}$ (*red*); and (1/2) [halothane]$_{max}$ (*blue*); [halothane] = zero after the final purge (*cyan*). Juxtaposed above the profiles is a schematic representation of the Langmuir monolayer of hbAP1 peptide bundles, approximately to scale.

the air-water interface onto the coordinate axis, z, perpendicular to the plane of the interface. The electron density profile is averaged spatially over the plane of the monolayer azimuthally about the z axis, and temporally over the time of the data collection, varying from a few seconds to ~1 min per data-point. Fig.S8 shows the 2–3 profiles obtained sequentially from that same hbAP1 monolayer at each of four different experimental conditions, as well as the corresponding 1–2 difference profiles between successive profiles at each condition. The phased Fourier transform in the algorithm resulting in these profiles is necessarily truncated for momentum transfer values exceeding q_z^{max}, the point beyond which the Fresnel-normalized reflectivity data from the peptide monolayer at the water-helium interface becomes identical to that for the interface in the absence of the peptide monolayer to within the photon counting-statistics noise level. Truncation of the transform at $q_z^{max} \approx 0.5$ Å^{-1} in this work results in the profiles containing a low amplitude, high-frequency component (or "ripple") of wavelength ~15Å (defining the "spatial resolution" of the profiles), whose mean value defines the local average electron density over any particular region of the profile exceeding this minimum wavelength. The 2–3 electron-density profiles calculated for the monolayer at each condition can be seen to be identical to within the amplitude of this high-frequency ripple over the entire extent of the monolayer profile in Fig. S8. The difference electron-density profiles calculated between two successive profiles at each condition exhibit only the high-frequency ripple component fluctuating about a mean of zero, or near zero, electron density over the entire extent of the monolayer profile, the amplitude of these fluctuations being less than the twice the amplitude of those in each profile, once equilibration at each condition has been fully achieved. Thus, for difference profiles calculated between two profiles for which the monolayer is fully equilibrated at two different conditions to be significant, they must therefore exhibit features of greater amplitude and lower frequency than those evident in this figure.

Inspection of the electron-density profiles reveals features common to all the profiles. The profile obtained before the introduction of halothane exhibits a rise in electron density from the (zero) density of the vapor phase to that of the monolayer with the peptide/vapor interface arbitrarily positioned at $z = 0$ Å, a region of nearly constant density extending to about $z = -50$ Å, and then a transition to the density of the aqueous subphase (0.333 e^-/Å^3, which becomes 1 in the reduced electron-density profiles $\rho(z)/\rho_{H2O}$ as shown) representing the peptide/subphase interface. The center of this latter interfacial feature in the profiles is near $z = -60$ Å, consistent with the expected length of the peptide, comprised of 37-residue α-helices with a 3-residue flexible loop. The uniformity of the electron density over the central portion of the profile structure indicates that virtually all of the peptides in the monolayer are oriented with their long axes normal to the air-water interface. There are also differences between the profiles

obtained under different conditions. The thickness of the monolayer does not change as halothane is introduced, but the density increases as the concentration of halothane increases. A more subtle difference is that both the interface between the monolayer and the subphase and the interface between the monolayer and the superphase become sharper. This makes the density in the central region more constant over a broader region and while also increasing the density in a narrow region closest to the superphase. Because these effects are apparent in all the profiles that have been exposed to maximal halothane, we obtain the most consistent results by comparing the profiles obtained in the presence of halothane with the profile obtained after halothane has been purged from the sample chamber (see Discussion). As the amphiphilic 4-helix bundle peptide is retained in the monolayer at constant area/helix during the experiment, the changes in electron density within the monolayer electron-density profile are assumed to arise primarily from the introduction of the electron-dense halothane into the monolayer (see below).

Computing differences between the electron-density profiles of the hbAP1 monolayer obtained at different concentrations of halothane allows us to visualize better the changes due to halothane and to quantify them (Fig. 2). These differences show that different parts of the peptide bundle have differing affinities for halothane. The difference between the profiles at [halothane]$_{max}$ and [halothane] $= 0$ after the final purge, namely the distribution of maximal halothane bound to the monolayer in this first set of experiments, shows that halothane is broadly distributed nearly uniformly across the entire length of the bundle. However, the difference between the profiles at [halothane]$_{max}$ and (1/2)[halothane]$_{max}$, which corresponds to the halothane removed in the first purge, is strongly asymmetrically distributed with a larger fraction of the halothane removed from the region $-25 < z < 0$ Å occupied by the hydrophobic domain of the bundle, and the remainder removed from the hydrophilic domain over the region $-60 < z < -25$ Å. Conversely, the difference between the profiles at (1/2)[halothane]$_{max}$ and 0, corresponding to the halothane removed in the second and final purge in this set of experiments, shows a broad symmetric distribution centered at $z = -35$ Å. So in this first set of dissociation experiments, halothane is initially present throughout the bundle at the highest concentration of halothane. During the first purge, most of the halothane present in the hydrophobic domain nearest the vapor phase, and some of the halothane present in the hydrophilic domain of the bundle leaves. The halothane remaining after the first purge is symmetrically distributed about a point near the center of the bundle in the vicinity of the designed cavity. All of these differences contain larger amplitude, low-frequency components compared to the differences between profiles obtained at each of the same concentrations of halothane after the structure stabilized (see Discussion). As a representative example, the difference between the first two reflectivity scans collected at [halothane]$_{max}$ also appears in Fig. 2 d.
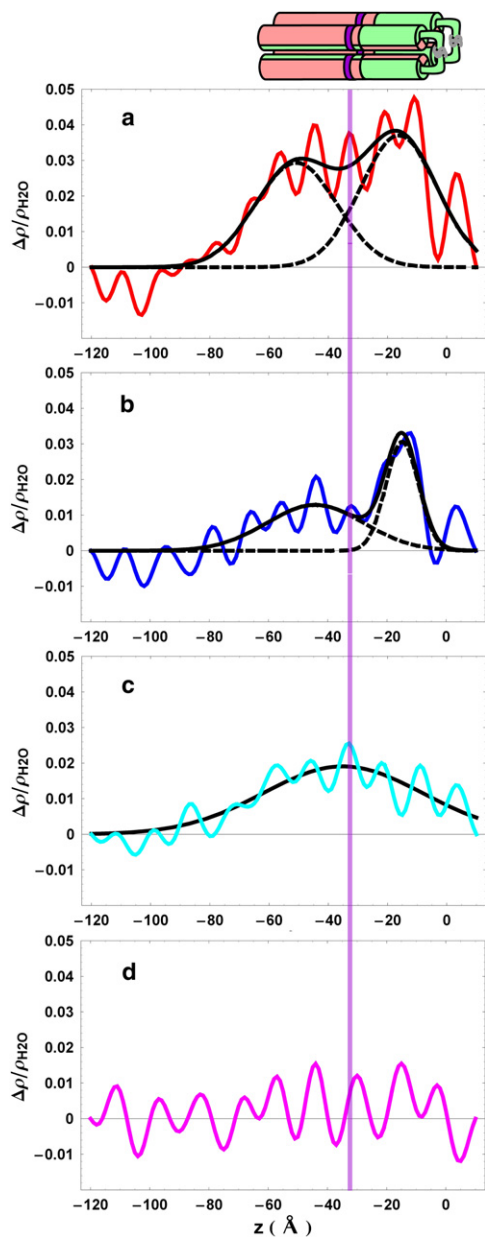
FIGURE 2 Differences between the electron-density profiles for the hbAP1 monolayer shown in Fig. 1 for the different halothane concentrations: (a) [halothane]$_{max}$ − [zero]; (b) [halothane]$_{max}$ − (1/2) [halothane]$_{max}$; and (c) (1/2)[halothane]$_{max}$ − [zero]. (d) The difference between electron-density profiles obtained from two successive reflectivity scans at the same concentration, [halothane]$_{max}$, shows the level of uncertainty in the differences arising from truncation errors (see Discussion and Fig. S8). Dashed black curves show the nonlinear least-squares fits of Gaussian functions to the difference profiles, with a black solid curve representing the sum of the Gaussians when two were used. The violet stripe running through the figures indicates the expected position of Ala[19], the residue forming the designed binding cavity for halothane, illustrated schematically in the model juxtaposed above the figure.

The subsequent second set of experiments used a different trough, increasing the steady-state level of [halothane]$_{max}$ and resulting in the introduction of more halothane into the

peptide bundles. Fig. 3 shows the electron-density profiles obtained from an hbAP1 monolayer using the later setup. The ordinate scale of the difference profiles (Fig. 4, *left side*) makes it clear that roughly twice as much halothane is present in the monolayer for these measurements as for the first set (Fig. 2). The difference between the profiles at [halothane]$_{max}$ and [halothane] = 0 after the final purge, namely the distribution for this higher maximal concentration of halothane bound to the monolayer in the second set of experiments, shows that halothane is again broadly distributed across the entire length of the bundle, but asymmetrically with an even larger amount within the hydrophobic domain (Fig. 4 *a*). The latter arises, most likely, from the available nonpolar environment of the space between the closely packed hydrophobic domains of the bundles within the monolayer adjacent the gaseous superphase. These difference profiles show that after this higher maximal concentration of halothane in the bundle, halothane leaves the hydrophobic domain and subphase end of the hydrophilic domain of the bundle and becomes more concentrated in the center of the bundle as a result of the first purge (Fig. 4 *b*). Again, most, but not all, of the halothane remaining after the first purge is symmetrically distributed about a point near the center of the bundle in the vicinity of the designed cavity; although there is more halothane within this distribution than for the prior set of experiments based on the electron-density level, and some halothane remains within the hydrophobic domain (Fig. 4 *c*).

Results from a monolayer of the control peptide, hbAP1 (A19L) possessing no cavity, using the later setup for the second set of experiments, also show changes due to the presence of halothane in the monolayer, but with a distinctly different pattern of dissociation during the stepwise purge. Fig. 4 (*right side*) shows differences between the electron-density profiles obtained at different concentrations of
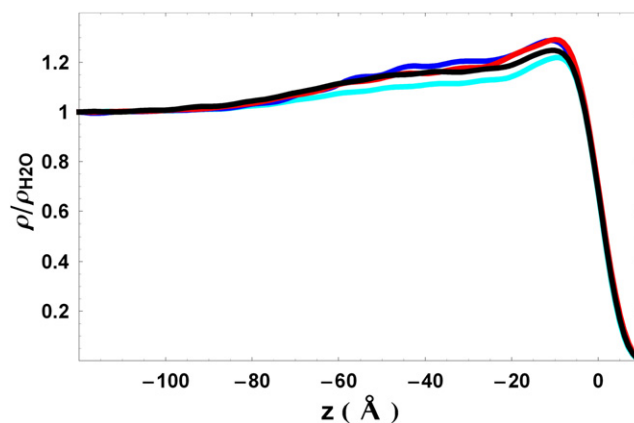

FIGURE 3 Electron-density profiles of the hbAP1 monolayer at the different concentrations of halothane established in the second set of dissociation experiments. Prehalothane (*black*), maximal halothane of [halothane]$_{max}$ (*red*); (1/2) [halothane]$_{max}$ (*blue*); and [zero] halothane after the final purge (*cyan*). [halothane]$_{max}$ is ~2-fold higher than that for the first set shown in Fig. 1.
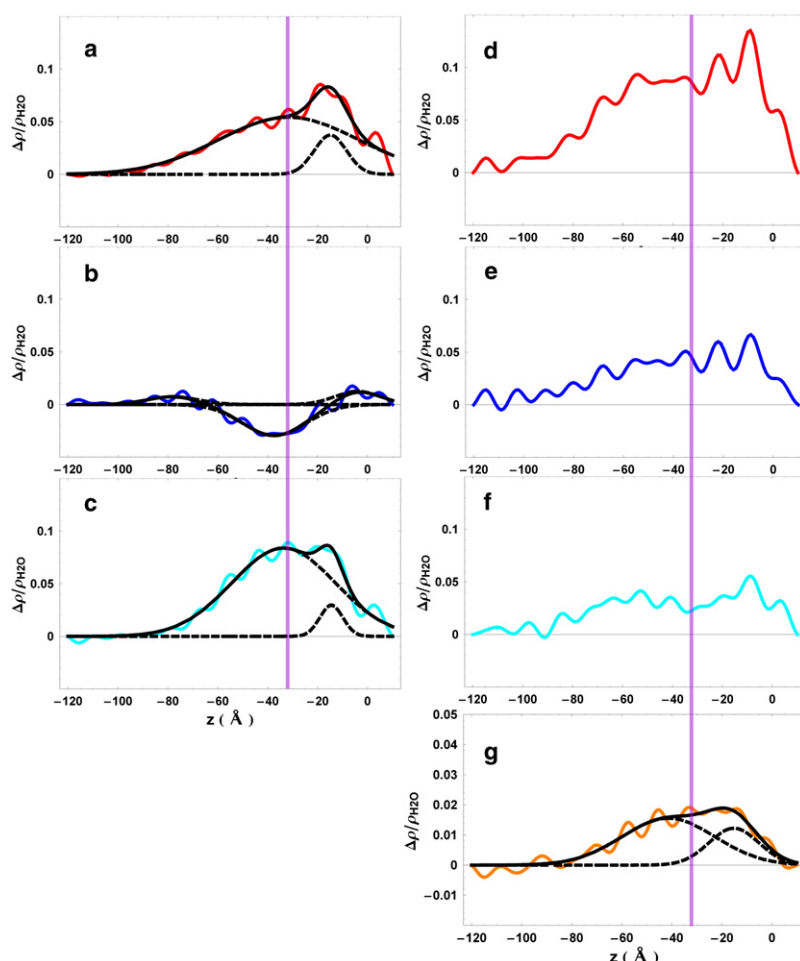
FIGURE 4 Differences between the electron-density profiles for the hbAP1 monolayer shown in Fig. 3 for the different halothane concentrations: (a) [halothane]$_{max}$ − [zero]; (b) [halothane]$_{max}$ − (1/2) [halothane]$_{max}$; and (c) (1/2) [halothane]$_{max}$ − [zero]. Differences between the profile structures of the control hbAP1(A19L) peptide monolayer shown in Fig. 5: (d) [halothane]$_{max}$ − [zero]; (e) [halothane]$_{max}$ − (2/3) [halothane]$_{max}$; (f) (2/3) [halothane]$_{max}$ − (1/3) [halothane]$_{max}$; and (g) (1/3) [halothane]$_{max}$ − [zero]. Dashed black curves show the nonlinear least-squares fits of Gaussian functions to the difference profiles, with a black solid curve representing the sum of the Gaussians when two were used. The stripe running through the figures indicates the expected position of residue 19, which is an Ala residue forming the designed binding cavity for halothane in hbAP1 and a Leu in the control peptide hbAP1(A19L).

halothane that are all effectively uniform over the length of the peptide bundle (only the profiles themselves are shown in Fig. 5). Measurements for the control peptide in this second set of experiments included a third purge that reduced the amount of halothane present to a quantity comparable to that for hbAP1 in the first set of experiments. (Compare Fig. 4 g with Fig. 2, and note that they have the same ordinate scale.) However, even though the amplitude of the difference profile shown in Fig. 4 g is comparable to the difference in Fig. 2 c, the distributions are still distinctly different. The distribution of halothane in the control peptide at this final purge (Fig. 4 g) is similar to the distribution of the maximal halothane present in the earlier hbAP1 measurement (Fig. 2 a), namely effectively uniformly distributed over the length of the bundle and not distributed symmetrically about a single point as in the final purge of the hbAP1 peptide (Fig. 2 c). So although the distribution of halothane in hbAP1(A19L) at [halothane]$_{max}$ is similar to that for hbAP1, namely a uniform distribution along the bundle, the intermediate results from the stepwise purges of halothane do not show any evidence that any part of the hbAP1(A19L) peptide bundle has a higher affinity for halothane than any other part. In particular, note that the presence

of residues with aromatic side-chains, Trp[15] and Phe[12], in this control peptide does not result in any localization of halothane along the length of the bundle.
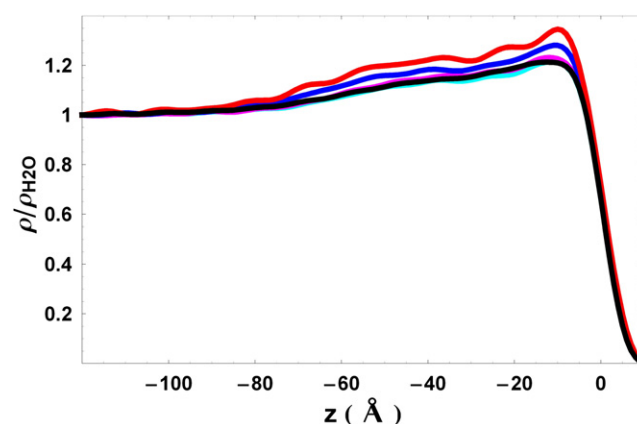

FIGURE 5 Electron-density profiles of the hbAP1(L19A) monolayer at the different concentrations of halothane established in the second set of dissociation experiments. Prehalothane (black), maximal halothane of [halothane]$_{max}$ (red), (2/3) [halothane]$_{max}$ (blue) (1/3) [halothane]$_{max}$ (magenta), and [zero] halothane after the final purge (cyan). [halothane]$_{max}$ is ~2-fold higher than that for the first set shown in Fig. 1.

DISCUSSION

Our approach is based on the analysis of the electron-density profiles obtained for each Langmuir monolayer of an amphiphilic 4-helix bundle peptide as it is subjected to a sequence of experimental conditions, namely before exposure to halothane, followed by exposure to a maximal concentration of halothane vapor in the superphase, and subsequently to stepwise purging of the halothane in the superphase back to zero concentration. Difference electron-density profiles calculated for any two profiles for which the monolayer was equilibrated at any one particular condition exhibited only the high-frequency ripple component fluctuating about a mean of zero, or near-zero electron density, over the entire extent of the monolayer profile, the amplitude of these fluctuations being less the twice the amplitude of those in each profile. These difference profiles at any one particular condition thereby establish the level of uncertainty in such difference profiles.

For difference electron-density profiles calculated for any two profiles for which the monolayer was equilibrated at two different conditions to be deemed significant, they must therefore contain lower frequency features of wavelength greater than that of the high-frequency truncation ripple whose amplitude exceeds twice the amplitude of this ripple present in each profile. Importantly, having at least two profiles fully equilibrated at each condition provides a minimum of four (2^2) independent difference electron-density profiles between any two different conditions. The high degree of similarity of such significant features among these four independent difference profiles for all of the cases described in this work clearly demonstrate the reproducibility or robustness of these features.

As noted in Results, comparison of the electron-density profiles for the peptide monolayer fully equilibrated before exposure to maximal halothane with those after exposure to maximal halothane and subsequently purged stepwise to zero halothane concentration shows a small but significant irreversible effect of halothane exposure on the monolayer structure. This comparison suggests that exposure to maximal halothane results in a better interbundle ordering within the monolayer. Specifically, all helices become perpendicular to the water-air interface resulting in the profiles becoming more perfectly uniform over the helices' expected 60 Å length and all bundles become more in-register over the monolayer plane, thereby significantly sharpening particularly the peptide-water interface and the peptide-gas interface at either end of the bundle. As a result of this reproducible effect of maximal halothane exposure on interbundle ordering within the monolayer, we have more closely examined only comparisons between the electron-density profiles obtained at finite concentrations of halothane with those obtained at zero halothane concentration achieved after stepwise purges from maximal halothane concentration.

Integration of the difference electron-density profiles in Figs. 2 and 4 allows an estimate of the amount of halothane present in the peptide monolayer. The scale for these results arises from a comparison of the electron densities of halothane and water. Each halothane molecule has 92 electrons in a characteristic volume of 123 Å^3 (7,21), and the 10 electrons of each water molecule occupy a characteristic volume of 27.8 Å^3 (21). With the monolayer maintained at a constant area of 100 Å^2/helix during the reflectivity measurements, the in-plane density of protein in the monolayer remains constant and only water, halothane and helium are free to leave the monolayer and equilibrate with the aqueous subphase below and the gaseous superphase above the monolayer. (We do not expect halothane to affect the distribution of the ions present in the buffered subphase.) Each halothane molecule that enters the monolayer could displace 4.43 water molecules, resulting in a net increase of 47.7 electrons in the monolayer. This assumption will result in the integration producing a maximal number of halothane molecules per bundle. However, the nonpolar core of the hydrophilic domain in such 4-helix bundles is very dynamic, as established by NMR studies and molecular dynamics simulations (9,14,22), and some space may also remain available between the closely packed hydrophobic domains in the monolayer. Thus, halothane could displace only vacuum or helium instead of water, thereby resulting in an overestimate in the number of halothane molecules per bundle, but by less than a factor of 2.

Considering the hbAP1 measurements at lower maximal halothane concentration achieved in the first set of experiments (with profile structures shown in Fig. 1), integration of the differences between profile structures obtained at the same concentration of halothane shows values of 0 ± 5 e/helix, so we can consider this the noise level in these estimates. This uncertainty can be expressed in terms of halothane as 0 ± 0.1 halothane/helix, or because these are 4-helix bundles, 0 ± 0.4 halothane/bundle. Integrating the differences between profile structures for the monolayer under different concentrations of halothane shows much larger differences in the number of electrons/helix. Relative to the profile structure at [halothane] = 0, the hbAP1 monolayer at [halothane]$_{max}$ contains ~70 excess electrons/helix, corresponding to ~1.6 halothane molecules/helix, or ~6–7 halothanes/bundle. Roughly 40% of these electrons (about three halothane molecules) leave the monolayer in the first purge, leaving 3–4 halothane molecules/bundle symmetrically distributed about a single maximum (Fig. 2 c). The second set of experiments with higher concentrations of maximal halothane achieved as many as 12–18 halothane molecules/bundle for hbAP1 and hbAP1(A19L) at [halothane]$_{max}$, and as few as ~3 halothane molecules/bundle for the hbAP1(A19L) monolayer at the last purge.

Fitting simple curves to the significant features (as defined above) within the difference electron-density profiles helps also to better quantify spatial aspects of the halothane distribution within the monolayer. Either a symmetric unimodal distribution, represented by a single Gaussian function, or a symmetric (or asymmetric) bimodal distribution, represented

by the sum of two Gaussians, can describe the main features of the difference profiles in most cases for the hbAP1 monolayer. We used both a global chi-squared parameter and the uniform distribution of residuals over the profile coordinate to establish the goodness of these fits. The fitting algorithm provided both the mean values of the parameters and their uncertainties for the so-fitted one or two Gaussian functions. Considering the first set of experiments for hbAP1 (Fig. 2), the difference between the profiles at [halothane]$_{max}$ and [halothane] = 0 representing the distribution of halothane along the bundle at maximal halothane achieved in the first set of experiments, can be approximated by a mildly asymmetric bimodal distribution, the two Gaussians of nearly equal amplitudes and widths summing to provide a fairly uniform distribution of halothane along the length of the bundle. The halothane that leaves during the first purge can be represented by a strongly asymmetric bimodal distribution that has a narrower component centered about $z_1 = -14.5$ Å within the hydrophobic domain and a broader component centered about $z_2 = -38$ Å within the hydrophilic domain. The areas of the two components are nevertheless comparable. The halothane that leaves during the second purge can be fit with a symmetric unimodal distribution, the single broad Gaussian centered about $z = -35 \pm 1$ Å. Locating residue Cys40 at the air/water interface ($z = 0$ Å), and treating all the residues according to the expected rise/residue in an α-helix of 1.5 Å, we expect Ala[19] to be between $-33 < z < -31.5$ Å. The observed center of the halothane distribution is very close to the expected position of Ala[19] but shifted slightly in the direction of Trp[15] (expected to be at $-39 < z < -37.5$ by the same logic). The full 1/e width of the distribution, 76 ± 3 Å, is much broader than the spatial resolution of the experiment. By comparison, in a resonance x-ray reflectivity measurement on a Langmuir monolayer with a covalently bound resonant atom, 2-bromo-stearic acid, the contribution of the resonant Br atom could be localized as a single Gaussian with a full 1/e width of ~8 Å ($2\sqrt{2}\sigma$, $\sigma = 3$ Å), namely about the same as the observed roughness of a clean air-water interface (15). In that experiment, the range over which data was collected was about the same, but significant components of the data existed out to somewhat higher $q_z = 0.6$ Å^{-1}. Thus, if the hbAP1 peptide bundles in the Langmuir monolayer were to contain a single halothane very tightly bound with a well-defined position along the length of the bundle, we would expect to see a distribution not much larger than the expected size of the halothane molecule (e.g., ~7 Å). Because all of the bundles are effectively identical, both in their composition and their location/orientation with respect to the water-air interface, the broad distribution is mostly likely dynamic in origin, with halothane showing an increased probability to be localized about the site of the designed binding cavity, but nevertheless capable of translational motion along the core of the bundle.

Even though our dissociation experiments did not study the peptide-halothane complex at a stoichiometry of 1 halothane/4-helix bundle, we see evidence after the first purge of halothane from the hbAP1 monolayer that the remaining 3–4 halothanes left in the bundle are distributed with the maximum probability centered on the site of Ala[19], whose small side chains were intended to form the binding cavity in the bundle. In contrast, the measurements with the control peptide hbAP1(A19L) after two purges reach only approximately three halothanes/bundle, but this smaller amount of halothane still is not localized at a single site in the bundle. The distribution of these halothane molecules over the length of the hbAP1(A19L) bundle can be fit with a mildly asymmetric bimodal distribution like that for hbAP1 at six to seven halothane molecules per bundle, the two Gaussians summing to provide a fairly uniform distribution of halothane along the length of the bundle. Thus, these dissociation experiments provide the first direct structural evidence in support of this approach to designing anesthetic binding cavities since the photoaffinity labeling results for soluble peptides (8).

The behavior of hbAP1 in the second set of dissociation experiments deserves some further comment. The results from the first set of experiments for hbAP1 at the maximal level of halothane incorporated into the monolayer indicated a nearly uniform distribution of halothane over the length of the bundle, effectively modeled as a mildly asymmetric bimodal distribution, at six to seven halothane molecules per bundle, as described above. It then may seem surprising that the first purge in the second set results to first approximation in a near unimodal distribution of halothane centered about the designed cavity location, even though the halothane concentration in the monolayer was at a somewhat higher level than six to seven molecules/bundle. However, the distribution is obviously bimodal in fact with a substantial second component within the hydrophobic domain, and this may provide a second indication that our protocol has not allowed sufficient time to fully establish an equilibrium situation, despite the invariance achieved for successive reflectivity scans at each halothane concentration to within the experimental noise level. Nevertheless, this result may be an indication that the somewhat higher affinity of the designed cavity for halothane within hbAP1, compared with the nonpolar core of the bundle, can tend to localize halothane in the vicinity centered about the position of the cavity even at higher concentrations within the bundle when challenged with a purge under nonequilibrium conditions. Again, it is important to note that the control peptide lacking only the cavity exhibited only an essentially uniform distribution of halothane over the entire length of the bundle, with no such evidence of any localization under otherwise identical conditions when challenged with purges at these higher halothane concentrations within the bundle.

One aspect of the work described above has recently been improved via a halothane "association" experiment. Instead of exposing the peptide monolayer to maximal halothane in the moist helium atmosphere above the monolayer followed by a stepwise purge, we exposed a fully equilibrated

monolayer of hbAP1 to a halothane concentration anticipated to result in closer to only one molecule per bundle based on the previous experiments. After equilibration at that lower concentration, the halothane in the atmosphere was again subsequently purged to zero. The difference electron-density profile calculated between the electron-density profile for the monolayer fully equilibrated at that lower halothane concentration and that after the purge is shown in Fig. 6. Integration of this difference profile indicated that the average halothane concentration per 4-helix bundle was indeed only slightly greater than one (e.g., ~1.1). This difference profile is asymmetric, has narrower full-width, and is more peaked compared to the symmetric difference profile for three to four halothane molecules per bundle shown in Fig. 2 c. Specifically, the full-width of the difference profile at about one halothane molecule per bundle is only ~42 Å compared with ~76 Å at three to four halothane molecules per bundle. At about one halothane per bundle, the halothane distribution is more peaked due to narrow component centered at $z \sim -36 \pm 2$ Å, also near the expected location of the cavity long the length of the bundle, with a full-width of only $2\sqrt{2}\sigma \sim 19 \pm 3$ Å. This suggests that the halothane is becoming even more localized to the near vicinity of the cavity along the length of the bundle as the average halothane/bundle stoichiometry is reduced. Nevertheless, the width of the distribution even within this narrower component still exceeds halothane's diameter by a factor of ~2–3. Importantly, analogous difference electron-density profiles for the control peptide hbAP1(A19L) still show only a nearly uniform distribution of halothane over the entire length of the bundle, even at this lower level of halothane in the monolayer achieved in these association experiments. Finally, similar results were obtained in these association experiments utilizing hbAP-Phe$_{CN}$, a mutant of the hbAP1 peptide utilized in parts II and III under this title in which Trp[15] was replaced by cyano-phenylalanine to thereby enable an investigation of halothane binding via infrared spectroscopy (see Fig. 6).

In future work, we plan to utilize a newly developed interferometric technique, using an inorganic, solid multilayer reference structure in the aqueous subphase positioned sufficiently close to (e.g., to within 50–100 Å), but not in contact with the peptide monolayer. This will provide for a substantial enhancement in sensitivity to the presence of halothane within the profile structure of the model ion channel protein and a substantial extension in the spatial resolution of the profile to well below 10 Å (V. Krishnan, J. Strzalka, J. Liu, C. Liu, I. Kuzmenko, T. Gog, and J. K. Blasie, unpublished data).

CONCLUSIONS

The simplicity of the lipid-free model membrane protein system, vectorially oriented in Langmuir monolayers at the air-water interface, allows us to unambiguously study the protein/anesthetic interaction. This interaction showed different characteristics depending on the peptide and the
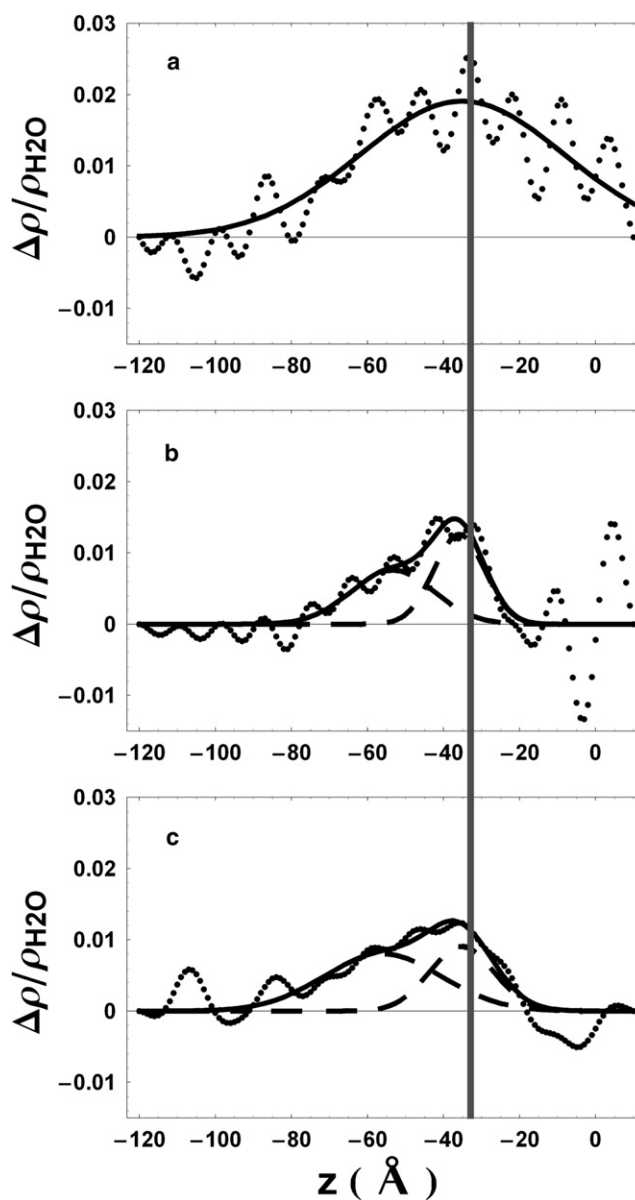

FIGURE 6 Differences (*dotted lines*) between the electron-density profiles for the hbAP1 and hbAP-PheCN monolayers at different halothane concentrations in the recent association experiments. (*a*) (1/2) [halothane]max − [zero] for hbAP1 from the dissociation experiment shown in Fig. 2 *c* and again here for comparison. (*b*) [Halothane]one/bundle − [zero] for hbAP1; and (*c*) [halothane] one/bundle − [zero] for hbAP-PheCN. [Halothane]one/bundle denotes the concentration of ~1–1.5 halothane molecules per 4-helix bundle achieved in the association experiments. The black dashed curves show the nonlinear least-squares fits of Gaussian functions to the difference profiles, with a black solid curve representing the sum of the Gaussians when two were used. The gray stripe running through the figures indicates the expected position of Ala[19], the residue forming the designed binding cavity for halothane. The lower concentration of approximately one halothane molecule per bundle achieved in the association experiments results in no halothane remaining in the hydrophobic domain extending over $-20\text{Å} < z < 0\text{Å}$. The additional features near the peptide-gas interface at $z = 0$ Å in the difference profile shown in panel *b* arise from the reversible effect of halothane on the width of the peptide-gas interface in this association experiment with hbAP1. The full-width of the halothane distribution for hbAP1 in panel *b* was calculated from the best-fit parameters of two Gaussian functions as $(z1 - z2) + \sqrt{2}(\sigma_1 + \sigma_2)$. See Discussion for further details.

relative concentration of halothane. In the control peptide, and in the target peptide possessing a designed cavity, at higher concentrations, halothane was found to be present throughout the length of the bundle, associating with the residues forming the core of the bundle. In the target protein at lower concentrations of halothane, the distribution of halothane became localized in a broad unimodal distribution centered about the Ala residues specifically designed to form a cavity for binding anesthetics in the core of the bundle. This rich behavior follows as a consequence of the thermodynamics discussed previously, where the dissociation constant of the peptide for halothane is so large that the energetics of the association are only marginally better than those implied by the partition coefficient of the anesthetic into a nonpolar medium. Because the dissociation constant of these model peptides is close to the range of physiologically relevant anesthetic concentrations, it is likely that this weak association interaction is shared by many proteins in vivo. The ability of x-ray reflectivity to detect and locate halothane within the profile structure of the monolayer despite the inherent disorder of the ligand in the system underlines its advantages over other techniques for structural characterization. For example, solution-based NMR and especially x-ray crystallography are not capable of detecting protein ligands with such inherent positional disorder.

This study also establishes the viability of our model membrane protein system for studying anesthetic-protein interactions, suitable as a platform for other complementary techniques. These synthetic peptides can easily accommodate nonbiological amino acids serving as labels for polarized infrared spectroscopic measurements on oriented samples. For instance, cyano-phenylalanine has already been substituted for the Trp in hbAP1 and used to probe the local interactions between halothane and the amino-acid residues via fluorescence and polarized vibrational spectroscopy in samples that have also been similarly characterized structurally by x-ray scattering (13). Interpretation of the results was enabled by utilization of molecular dynamics simulations affording a three-dimensional view of the peptide structure at atomic resolution otherwise unattainable experimentally (14). Similarly, deuterium-labeled amino acids can also be incorporated into the peptides at specific sites and neutron reflectivity studies of monolayers prepared from a family of ^{2}H-labeled but otherwise isomorphous peptides could allow determination of the positions of individual residues within the profile structure of the monolayer (23). These positions could in turn validate or constrain molecular dynamics simulations yielding three-dimensional structures consistent with the projections observed in the reflectivity measurements.

SUPPORTING MATERIAL

Figures S1–S8 referenced in the text are available at http://www.biophysj.org/biophysj/supplemental/S0006-3495(09)00608-0.

REFERENCES

1. Koblin, D. D. 2001. Structure-activity relationships of inhaled anesthetics. In Molecular Bases of Anesthesia. E. Moody and P. Skolnick, editors. CRC Press, Boca Raton, FL. 123–145.

2. Dilger, J. P. 2001. Basic Pharmacology of Volatile Anesthetics. In Molecular Bases of Anesthesia. E. Moody and P. Skolnick, editors. CRC Press, Boca Raton, FL. 1–35.

3. Franks, N. P., and W. R. Lieb. 1994. Molecular and cellular mechanisms of general-anesthesia. Nature. 367:607–614.

4. Miyazawa, A., Y. Fujiyoshi, M. Stowell, and N. Unwin. 1999. Nicotinic acetylcholine receptor at 4.6 angstrom resolution: transverse tunnels in the channel wall. J. Mol. Biol. 288:765–786.

5. Liu, R. Y., P. J. Loll, and R. G. Eckenhoff. 2005. Structural basis for high-affinity volatile anesthetic binding in a natural 4-helix bundle protein. FASEB J. 19:567–576.

6. Robertson, D. E., R. S. Farid, C. C. Moser, J. L. Urbauer, S. E. Mulholland, et al. 1994. Design and synthesis of multi-heme proteins. Nature. 368:425–431.

7. Johansson, J. S., B. R. Gibney, F. Rabanal, K. S. Reddy, and P. L. Dutton. 1998. A designed cavity in the hydrophobic core of a four-alpha-helix bundle improves volatile anesthetic binding affinity. Biochemistry. 37:1421–1429.

8. Johansson, J. S., D. Scharf, L. A. Davies, K. S. Reddy, and R. G. Eckenhoff. 2000. A designed four-alpha-helix bundle that binds the volatile general anesthetic halothane with high affinity. Biophys. J. 78:982–993.

9. Cui, T. X., V. Bondarenko, D. J. Ma, C. Canlas, N. R. Brandon, et al. 2008. Four-alpha-helix bundle with designed anesthetic binding pockets. Part II: halothane effects on structure and dynamics. Biophys. J. 94:4464–4472.

10. Ye, S. X., J. Strzalka, I. Y. Churbanova, S. Y. Zheng, J. S. Johansson, et al. 2004. A model membrane protein for binding volatile anesthetics. Biophys. J. 87:4065–4074.

11. Lear, J. D., Z. R. Wasserman, and W. F. Degrado. 1988. Synthetic amphiphilic peptide models for protein ion channels. Science. 240:1177–1181.

12. Churbanova, I. Y., A. Tronin, J. Strzalka, T. Gog, I. Kuzmenko, et al. 2006. Monolayers of a model anesthetic-binding membrane protein: formation, characterization, and halothane-binding affinity. Biophys. J. 90:3255–3266.

13. Liu, J., J. Strzalka, A. Tronin, J. S. Johansson, and J. K. Blasie. 2009. Mechanism of interaction between the general anesthetic halothane and a model ion channel protein, II: fluorescence and vibrational spectroscopy using a cyanophenylalanine probe. Biophys. J. 96:4176–4187.

14. Zou, H., J. Liu, and J. K. Blasie. 2009. Mechanism of interaction between the general anesthetic halothane and a model ion channel protein: III. Molecular dynamics simulation incorporating a cyanophenylalanine spectroscopic probe. *Biophys. J.* 96:4188–4199.

15. Strzalka, J., E. DiMasi, I. Kuzmenko, T. Gog, and J. K. Blasie. 2004. Resonant x-ray reflectivity from a bromine-labeled fatty acid Langmuir monolayer. *Phys. Rev. E.* 70:051603.

16. Weiss, A. H., M. Deutsch, A. Braslau, B. M. Ocko, and P. S. Pershan. 1986. Novel x-ray diffractometer for liquid surface studies. *Rev. Sci. Instrum.* 57:2554–2559.

17. Braslau, A., P. S. Pershan, G. Swislow, B. M. Ocko, and J. Als-Nielsen. 1988. Capillary waves on the surface of simple liquids measured by x-ray reflectivity. *Phys. Rev. A.* 38:2457–2470.

18. Strzalka, J., X. X. Chen, C. C. Moser, P. L. Dutton, B. M. Ocko, et al. 2000. X-ray scattering studies of maquette peptide monolayers. 1. Reflectivity and grazing incidence diffraction at the air/water interface. *Langmuir.* 16:10404–10418.

19. Blasie, J. K., S. Zheng, and J. Strzalka. 2003. Solution to the phase problem for specular x-ray or neutron reflectivity from thin films on liquid surfaces. *Phys. Rev. B.* 67:224201.

20. WolframResearch 1999. Statistics 'NonlinearFit'. *In* Mathematica 4 Standard Add-on Packages. E. Martin and J. Novak, editors. Wolfram Media, Champaign, IL. 476–483.

21. Abraham, M. H., and J. C. McGowan. 1987. The use of characteristic volumes to measure cavity terms in reversed phase liquid-chromatography. *Chromatographia.* 23:243–246.

22. Ma, D. J., N. R. Brandon, T. X. Cui, V. Bondarenko, C. Canlas, et al. 2008. Four-alpha-helix bundle with designed anesthetic binding pockets. Part I: structural and dynamical analyses. *Biophys. J.* 94:4454–4463.

23. Strzalka, J., B. R. Gibney, S. Satija, and J. K. Blasie. 2004. Specular neutron reflectivity and the structure of artificial protein maquettes vectorially oriented at interfaces. *Phys. Rev. E.* 70:061905.